Available online at www.sciencedirect.com
SCIENCE DIRECT®
Journal of Computational Physics 207 (2005) 389–404
JOURNAL OF COMPUTATIONAL PHYSICS
www.elsevier.com/locate/jcp

A level-set approach for simulations of flows with multiple moving contact lines with hysteresis

Peter D.M. Spelt *

School of Mathematical Sciences, University of Nottingham, Nottingham NG7 2RD, UK

Received 19 May 2004; received in revised form 26 January 2005; accepted 26 January 2005
Available online 25 February 2005

Abstract

The level-set method of Sussman et al. [J. Comput. Phys. 148 (1999) 81] is extended such that flows with multiple moving contact lines can be simulated, accounting for inertia, a relation between contact-line speed and contact angle, slip and contact-line hysteresis. The convergence properties of the method are investigated, with particular attention on the resolution of the contact-line stress singularity. Results are compared with a lubrication theory for spreading droplets.

Keywords: Level-set methods; Two-phase flow; Moving contact lines; Hysteresis

1. Introduction

Incompressible two-phase flows with moving contact lines are common in a variety of applications, such as coating and biological processes (e.g. [21]). A difficulty of simulating such flows is that the Navier–Stokes equations for both fluids, in combination with no-slip boundary conditions, predict that an infinite force is required to move a contact line [6]. We shall follow here the approach in which this stress singularity is avoided by replacing the no-slip condition by the Navier condition for the velocity component U_1 along the entire wall [6]

$$U_1 = \lambda \frac{\partial U_1}{\partial x_2}, \tag{1}$$

* Present address: Department of Chemical Engineering and Chemical Technology, Imperial College London SW7 2AZ, UK.
E-mail address: p.spelt@imperial.ac.uk.

0021-9991/$ - see front matter
doi:10.1016/j.jcp.2005.01.016

where λ is the sliplength. Alternative approaches are to include microscopic (van der Waals) interactions between the fluids and the solid wall or a precursor film ahead of the moving contact line, or to use a diffuse interface (see [3,7,15,16,21] for a review of different approaches).

In addition to avoiding the stress singularity, the contact angle must be prescribed, or, alternatively, the contact-line speed. When prescribing the contact angle [12], the value of the angle is dependent on the sign of the contact-line speed U^{cl} because of hysteresis,

$$\begin{aligned} &\theta = \theta_{\mathrm{A}} && \text{if } U^{\mathrm{cl}} > 0, \\ &\theta = \theta_{\mathrm{R}} && \text{if } U^{\mathrm{cl}} < 0, \\ &\theta_{\mathrm{R}} \leqslant \theta \leqslant \theta_{\mathrm{A}} && \text{if } U^{\mathrm{cl}} = 0, \end{aligned} \tag{2}$$

where θ, θ_{A} and θ_{R} are the dynamic, advancing and receding contact angle, respectively [9]. A simple example of prescribing the contact-line speed is

$$U^{\mathrm{cl}} = \begin{cases} \kappa(\theta - \theta_{\mathrm{A}}) & \text{if } \theta > \theta_{\mathrm{A}}, \\ \kappa(\theta - \theta_{\mathrm{R}}) & \text{if } \theta < \theta_{\mathrm{R}}, \\ 0 & \text{otherwise.} \end{cases} \tag{3}$$

The merits of these approaches are discussed in [6,14].

A numerical simulation technique that includes (1) and (2) or (3) allows one to assess in practical applications whether contact-line motion is limited by slip or the contact-line speed/contact angle relation, and to what extent. Analytical approaches are usually restricted to thin film flows, such that lubrication arguments can be used, or to creeping flows.

At present, no simulation technique appears to be available for the problem of solving the equations of motion with inertia for both phases with (1) and (3). The problem was resolved only partly by Renardy et al. [22], who developed a volume-of-fluid method for moving contact lines with fixed dynamic contact angle. They accounted for slip, but such that λ was proportional to the grid spacing. It is unclear how their method can be extended to account for hysteresis (or for (3)). Other methods (e.g., the lattice-Boltzmann method of Kang et al. [17]) do not track the contact angle in time. Full numerical simulations of a droplet sliding down a wall in the creeping flow limit have been presented recently in [19]. In [19], effective slip was provided by discretisation errors, such that the sliplength is a function of grid spacing [20].

Promising results were obtained by Sussman and Uto [28] and Son et al. [26], who used a level-set approach for a single contact line, with constant contact angle, not accounting for slip. In the present paper, the level-set method of [27] is adapted to account for multiple moving contact lines, slip, and (3) (or (2)). The sliplength λ is an input parameter in the method proposed here. It is shown that the results for a given value of λ appear to be convergent with respect to the grid spacing. Results are compared with previous numerical and analytical work, and the regularisation of the stress singularity and the qualitative flow structure are analysed in Section 5. The validity of a macroscale approach for cases where λ is very small is investigated in Section 6.

2. Level-set method

Several level-set methods for incompressible two-phase flow have been proposed. The single-grid (two-dimensional) version of the method of [27] has been used here, because it allows for no-slip boundary conditions. Some modifications were made, in particular to ensure mass conservation and to allow standard software to be used, and these are discussed in this section.

The level-set function ϕ is taken as the signed distance function from the interface, the sign being used to distinguish between the two fluids; the zero level set corresponds to the fluid interface. The equations of

motion are written in a form that is valid throughout the entire domain, where the density and viscosity are functions of $\phi(\mathbf{x},t)$. The abrupt change in these fluid properties across the interface is smoothed out over a length that is proportional to the grid spacing. The action of surface tension is represented as a singular term in the momentum equation, also smoothed out over several mesh points. The equations of motion are solved using the variable density/viscosity method of [2]. At time t^n the level-set function $\phi^n_{i,j}$ and velocity components $\mathbf{U}^n_{i,j}$ are known and defined at cell centres, the pressure $p^{n-1/2}_{i+1/2,j+1/2}$ is defined at cell corners. A uniform Cartesian mesh is used. The timestep Δt is determined as in [27]. Each timestep consists of four steps (for details see [27]):

Step 1. *Level-set update for* ϕ, using the advection equation

$$\phi^{n+1} = \phi^n - \Delta t[\mathbf{U}\cdot\nabla\phi]^{n+1/2}. \tag{4}$$

The advection term on the right-hand side is evaluated using an explicit predictor–corrector scheme, that only depends on variables evaluated at the previous timestep. In a predictor step, $\mathbf{U}$ and ϕ at cell faces is obtained from Taylor-series expansions from either side of the cell face. An upwinding procedure is used as the correction step. The advection term is finally obtained from central differentiation. The cell-face velocity components are not necessarily divergence-free. A MAC projection (which involves solving a Poisson equation) can be applied to enforce incompressibility, which leads to somewhat improved convergence rates [2]. The MAC projection step was implemented, but it was not used for the results presented in this paper. The intermediate value of the level-set function is used to obtain

$$\rho^{n+1/2} = \rho_1 + (\rho_2-\rho_1)H_\epsilon(\phi^{n+1/2}), \quad \mu^{n+1/2} = \mu_1 + (\mu_2-\mu_1)H_\epsilon(\phi^{n+1/2}), \tag{5}$$

where for instance ρ_1 is the density of fluid 1. $H_\epsilon(\phi)$ is the smoothed Heaviside function

$$H_\epsilon(\phi) = \begin{cases} 0 & \text{if } \phi < -\epsilon, \\ \frac{1}{2}\left(1+\frac{\phi}{\epsilon}+\frac{1}{\pi}\sin(\pi\phi/\epsilon)\right) & \text{if } |\phi| \leqslant \epsilon, \\ 1 & \text{if } \phi > \epsilon. \end{cases} \tag{6}$$

The smoothing parameter ϵ is set to $1.5\Delta x$.

Step 2. *Semi-implicit viscous solve for* $\mathbf{U}^* = (U^*, V^*)$:

$$\frac{\mathbf{U}^*-\mathbf{U}^n}{\Delta t} = -[\mathbf{U}\cdot\nabla\mathbf{U}]^{n+1/2} - \frac{Gp^{n-1/2}}{\rho^{n+1/2}} + \frac{\mathscr{L}}{2\rho^{n+1/2}} - \frac{\mathscr{M}^{n+1/2}}{\rho^{n+1/2}} + \mathbf{g}. \tag{7}$$

Here, $\mathscr{L}$ and $\mathscr{M}$ are central-difference discretisations of the viscous and surface tension terms, respectively; Gp is an approximation to ∇p. Details of these discretisations can be found in [27]. In the present implementation, Crank–Nicholson is used for the normal viscous stresses only, i.e., $\mathscr{L} = (\mathscr{L}^* + \mathscr{L}^n)/2$ (the other viscous terms are treated explicitly), such that standard multigrid software could be used to solve (7) (with Neumann boundary conditions for $\mathbf{U}^* - \mathbf{U}^n$) down to machine accuracy. The advection term (first term on the right-hand side) is obtained using the same technique as for the advection term in (4).

Step 3. *Projection step for* $\mathbf{U}^{n+1}$ using

$$\frac{\mathbf{U}^{n+1}-\mathbf{U}^*}{\Delta t} = -\frac{Gq^{n+1/2}}{\rho^{n+1/2}}. \tag{8}$$

The scalar $q^{n+1/2}$ is obtained from

$$L_\rho q = D\left(\frac{\mathbf{U}^*-\mathbf{U}^n}{\Delta t}\right), \tag{9}$$

where D and L_ρ are the discretised divergence and density-weighted Laplace operators. The nine-point stencil for L_ρ used by [27] results from a variational form of the incompressibility condition (after

substitution of (8), cf. [2]), in which the pressure is approximated by a piecewise bilinear function on squares. Although requiring a non-standard multigrid technique, this was found to be especially suitable for large density ratios (such as air/water mixtures), for which the method used here may be rather slowly convergent. In the present work, relatively small density ratios will be used, and we have approximated the pressure as a piecewise linear function on triangles, which leads to the standard five-point finite difference Laplacian [2],

$$(\Delta x)^2(L_\rho q)_{i+\frac{1}{2},j+\frac{1}{2}} = -\left(\frac{1}{\rho_{i,j+1}}+\frac{1}{\rho_{i,j}}+\frac{1}{\rho_{i+1,j}}+\frac{1}{\rho_{i+1,j+1}}\right)q_{i+\frac{1}{2},j+\frac{1}{2}} + \left(\frac{1}{2\rho_{i+1,j}}+\frac{1}{2\rho_{i+1,j+1}}\right)q_{i+\frac{3}{2},j+\frac{1}{2}} + \left(\frac{1}{2\rho_{i,j}}+\frac{1}{2\rho_{i+1,j}}\right)q_{i+\frac{1}{2},j-\frac{1}{2}} + \left(\frac{1}{2\rho_{i,j+1}}+\frac{1}{2\rho_{i+1,j+1}}\right)q_{i+\frac{1}{2},j+\frac{3}{2}} + \left(\frac{1}{2\rho_{i,j+1}}+\frac{1}{2\rho_{i,j}}\right)q_{i-\frac{1}{2},j+\frac{1}{2}}$$

and a standard four-point discretisation of the right-hand side of (8). Almgren et al. [2] found only small differences between the results for variable-density flows. For cells adjacent to a solid wall at $j=\frac{1}{2}$, after setting the divergence of (8) equal to zero the no-penetration condition leads to

$$\frac{1}{\rho_{i,1}}\left(q_{i-\frac{1}{2},\frac{1}{2}}+q_{i+\frac{3}{2},\frac{1}{2}}-2q_{i+\frac{1}{2},\frac{1}{2}}\right)+\frac{1}{\rho_{i+1,1}}\left(q_{i+\frac{1}{2},\frac{3}{2}}+q_{i+\frac{3}{2},\frac{1}{2}}-2q_{i+\frac{1}{2},\frac{1}{2}}\right)=\frac{\Delta x}{\Delta t}\left(U^*_{i+1,1}-U^*_{i,1}+V^*_{i,1}+V^*_{i+1,1}\right). \quad (10)$$

We have solved (9) using standard multigrid software. It was verified that $\nabla\cdot\mathbf{U}$ decreases with Δx (approximately first order [2]). After solving (9), the pressure is updated:

$$p^{n+1/2}=p^{n-1/2}+q^{n+1/2}. \quad (11)$$

Step 4. *Redistance of* ϕ^{n+1}: For $\tau=0\ldots\epsilon$ solve

$$\frac{\partial d}{\partial\tau}=S(\phi)(1-|\nabla d|),\quad d(\tau=0)=\phi^{n+1}, \quad (12)$$

where τ is an artificial time and $S(\phi)$ is the sign function, and subsequently set ϕ^{n+1} equal to $d(\epsilon)$. It was found that the redistance method used by [27] leads to errors in the total mass of each fluid that increase with time. Russo and Smereka [23] have shown that this is caused by the upwind scheme not being truly upwind close to the interface, and proposed a fix for the problem. The present application requires long integration times, and the subcell fix of Russo and Smereka [23] has been used here. Hence,

$$d_{i,j}(\tau=(m+1)\Delta\tau)\equiv d^{m+1}_{i,j}=\begin{cases} d^m_{i,j}-(\Delta\tau)/(\Delta x)\left(\mathrm{sgn}(d^0_{i,j})|d^m_{i,j}|-D_{i,j}\right) & \text{if } (i,j)\in\Sigma_{\Delta x},\\ d^m_{i,j}-\Delta\tau\,\mathrm{sgn}(d^0_{i,j})G(\phi_{i,j}) & \text{otherwise,}\end{cases} \quad (13)$$

where $G(\phi_{i,j})$ is a second-order upwind discretisation of $|\nabla\phi|-1$, $\Sigma_{\Delta x}$ are the points within one grid point from the zero level set, and

$$D_{i,j}=\frac{(\Delta x)d^0_{i,j}}{\Delta d^0_{i,j}}, \quad (14)$$

with

$$\begin{aligned}\Delta d^0_{i,j}=\ &\max\{((d^0_{i+1,j}-d^0_{i-1,j})^2+(d^0_{i,j+1}-d^0_{i,j-1})^2)^{1/2}/2,\\ &|d^0_{i+1,j}-d^0_{i,j}|,|d^0_{i,j}-d^0_{i-1,j}|,|d^0_{i,j+1}-d^0_{i,j}|,|d^0_{i,j}-d^0_{i,j-1}|,\gamma\}.\end{aligned} \quad (15)$$

We have used here $\gamma=\Delta x$; smaller values were found to lead eventually (large t) to deviations in the interface shape. At points where $\Delta d^0_{i,j}=\Delta x$, (13)–(15) result in $d^{m+1}_{i,j}=d^m_{i,j}$. It was verified that the L_1 norm of the

error in d is second order if $\gamma = 0$ [23]. But $\gamma = \Delta x$ results in a lower rate, tests indicate approximately first order convergence.

Even after this modification, the total mass of each phase was not exactly conserved, and at long times, a slow increase in the area occupied by one of the phases was sometimes observed, in particular at large deformation of the interface. Therefore, at the end of each timestep, the area occupied by one fluid phase V and interface length S are determined from a piecewise linear reconstruction of the interface, and the level-set function at all points is then corrected using (as proposed by Sussman and Uto [28])

$$\phi = \phi + \frac{V - V_{\text{exact}}}{2S}, \tag{16}$$

where V_{exact} is the (constant) exact value of the area of the fluid phase considered. A similar correction was used in [24] for boundary-element simulations of similar problems.

It was verified that in systems with fixed contact lines, no contact-line motion occurs. In earlier implementations of the method, (16) was not used, and small velocity fluctuations were observed near the interface, even for a circular-cap-shaped drop on a wall in quiescent fluid. These small velocities (possibly generated by discretisation errors in the surface tension term in the momentum equations) would after a long integration time deform the interface. However, when using (16), these distortions are smeared out over the entire interface, and the interface remains stationary.

3. Boundary conditions for flows with moving contact lines

The slip condition (1) is applied along the entire wall with contact lines, following most analytical studies (e.g. [6]). For sufficiently small values of λ, this results in slip being only significant in close proximity of moving contact lines. The condition is applied by using a third-order discritisation of (1) to obtain U_1 at ghostpoints. The condition (2), or (3), is applied in the redistance step, using an iterative procedure at each artificial timestep (13). The results of this iterative procedure are values for $d_{i,j}$ at ghostpoints, and a new approximation for the position of contact lines, $x_1 = X^{\text{cl}}(t^{n+1})$. These steps (numbered **a**–**d**) are described in this section.

3.1. Determination of θ and $X^{cl}(t + \Delta t)$

Step a. First, the position of the interface at the height of the centres of the first two layers of cells adjacent to the wall (X^1 and X^2, respectively) is obtained from interpolation,

$$X^j = x_{i,j} + |\phi_{i,j}|/(|\phi_{i,j}| + |\phi_{i+1,j}|) \quad (\text{if } \phi_{i,j}\phi_{i+1,j} < 0), \tag{17}$$

$x_{i,j}$ is the coordinate along the wall of the cell centre (i,j).

Step b. If the contact-line speed is prescribed, the most-recent values of contact angles are used to obtain a first approximation of U^{cl} from (3): at the $(m + 1)$th redistance step (13), the contact angle value of the previous (mth) redistance step is used, or, at $m = 0$, the value from the previous timestep (at the first timestep, and $m = 0$, the contact angles are obtained from X^1 and a similar interpolation formula for X^{cl}). The position of a contact line at time t^{n+1}, $X^{\text{cl}}(t^{n+1})$, is then obtained from $X^{\text{cl}}(t^{n+1}) = X^{\text{cl}}(t^n) + U^{\text{cl}}\Delta t$. If (2) is used, $X^{\text{cl}}(t^{n+1}) = X^{\text{cl}}(t^n)$ at this stage.

Step c. The contact angle for each contact line is obtained from the results of steps **a** and **b**,

$$\sin\theta = \frac{\Delta x/2}{\sqrt{(X^1 - X^{\text{cl}})^2 + (\Delta x/2)^2}}. \tag{18}$$

This is used in all test problems discussed in this paper. Alternatively, X^2 can be used as well in other (higher-order) approximations (in some simulations presented in Fig. 9, $\tan\theta = \Delta x/(\frac{1}{5}X^1 + \frac{3}{5}X^2 - \frac{4}{5}X^{\mathrm{cl}})$ has been used). However, in order to obtain an overall method with more than first-order convergence properties, several other difficulties would have to be addressed (this is discussed in the next section). If the contact-angle is prescribed, it is first checked whether the resulting value of θ is outside $[\theta_{\mathrm{R}}, \theta_{\mathrm{A}}]$. If it is, θ is set to either θ_{A} or θ_{R}, as appropriate: if $\theta > \theta_{\mathrm{A}}$, then θ is set to θ_{A}; if $\theta < \theta_{\mathrm{R}}$, then θ is set to θ_{R}. X^{cl} is then changed accordingly, e.g., from $X^{\mathrm{cl}} = X^1 + \Delta\, x/(2\tan\theta)$ (consistent with (18)). At relatively large contact-line speed values, the interface is curved in a small area around the contact line, such that the angle between the interface and the horizontal changes for spreading drops from a maximum $\theta_{\max}$ just above the contact line to θ at the contact line. Therefore, in this paper, for cases without hysteresis, we have used a slight modification by using $X^{\mathrm{cl}} = X^1 + \Delta x/(\tan\theta + \tan\theta_{\max})$ (for cases with hysteresis, (18) would have to be made consistent with such modified expression for X^{cl}).

Steps **b** and **c** are repeated until θ has converged to within a small correction (typically 10^{-4}) of the previous iterative value. This procedure is carried out at each pseudo timestep in the redistance operation. For sufficiently small timesteps, $\theta(t^{n+1})$ and $X^{\mathrm{cl}}(t^{n+1})$ are close to their values at time t^n, and the iterative procedure may be expected to converge rapidly. Tests showed that $|\theta^i - \theta^{i-1}|$, where θ^i is the value of a contact angle after i iterations, is typically less than $0.01|\theta^{i-1} - \theta^{i-2}|$, so that only a few iterations are needed.

3.2. Prescription of ϕ at ghostcells

Once $\theta(t^{n+1})$ and $X^{\mathrm{cl}}(t^{n+1})$ have been determined in a pseudo timestep of the redistance operation (step 4 in Section 2), as outlined in Section 3.1, the value of $d_{i,j}$ at each ghostcell is determined such that it is consistent with the new contact angle and contact-line position. This is step **d** below, which is discussed in this section.

Boundary conditions should not be imposed on the level-set function for flows without contact lines, because during the redistance step, information travels along characteristics away from the interface towards the boundaries [23]. The value of the level-set function in ghostcells along such walls is therefore obtained from second-order extrapolation. From the same argument it follows, however, that when representing interfacial flow with contact lines by extrapolating the interface through the wall, a boundary condition should be imposed on walls with contact lines. Hence, for the left contact line shown in Fig. 1, the signal propagates away from the wall for any point left of that contact line, and a boundary condition (obtained from the distance to $\mathscr{L}_1$) at ghostpoints is required. For points far to the right of the right contact line, it is not possible to draw a normal to the nearest imaginary interfaces (dashed part of $\mathscr{L}_2$), the distance to be used should correspond to that from the solid part of the interface $\mathscr{L}_2$, and no boundary condition should be imposed on d (the value of d in ghostcells is therefore obtained from second-order extrapolation).

The two points P and Q in Fig. 1 indicate possible ghost-point locations between two contact lines. At P, a boundary condition is required for d. The value of d at P is should be set to the distance to the line $\mathscr{L}_1$. At

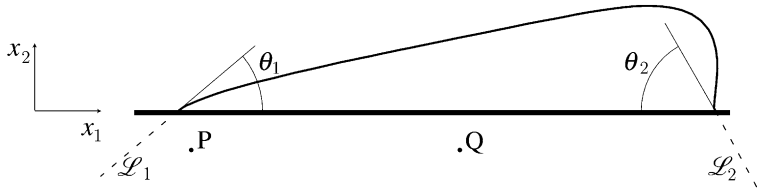

Fig. 1. For the simulation of (moving) multiple contact lines, interfaces that intersect with walls are extrapolated (indicated by the dashed lines). The distance to imaginary interfaces is used to determine boundary conditions for the level-set function.

Q, the minimum distance to an interface may be that to the solid part of $\mathscr{L}_1$, which can be obtained from extrapolation of d from the interior. Hence, the final step, after steps **a**–**c** in Section 3.1, is

Step d. The absolute value of $d_{i,0}$ at a ghost-cell location $\mathbf{x}_g = (x_{i,0} - \Delta x/2)$ is set to

$$|d_{i,0}| = \min\{D_{\text{extrapol}}, D_{\mathscr{L}_1}, D_{\mathscr{L}_2}\}, \tag{19}$$

where $D_{\text{extrapol}} = |2d_{i,1} - d_{i,2}|$ is an extrapolated value, and $D_{\mathscr{L}_k}$ is the distance between $\mathbf{x}_g$ and the extrapolated interface $\mathscr{L}_k$. Subsequently, the sign of $d_{i,0}$ is set such that it is consistent with which side of the interface $\boldsymbol{x}_g$ is located.

It was found that extrapolation should be used with some caution. For ghostpoints to the left of $\mathscr{L}_1$ in Fig. 1, where the distance $D_{\mathscr{L}_1}$ to the imaginary interface should be used, the extrapolated level-set function D_{extrapol} from a previous iterative step may happen to be less than this distance. As a result, the latter would be used instead (cf. (19)) ϕ was sometimes found to tend to zero for all ghostpoints to the left of $\mathscr{L}_1$. The cause of this instability has been eliminated by only using, at ghostpoints from where a normal can be drawn to an imaginary interface, an extrapolated value for d at ghostpoints located between the two contact lines.

3.3. Discussion

The linear extrapolation of d, as well as the straight-line extrapolation of the interface into the wall, can alter the curvature of the interface close to the contact line. The curvature is used in the source-term in the momentum equations (7), wherein it is multiplied by $\nabla H_\epsilon(\phi)$ [27]. In Fig. 2, the x_2-component of the source term is shown for a circular cap, with a prescribed contact angle (of 10°) equal to the angle between the circle and the horizontal.

Left of the contact line, the source term in the momentum equation is expected to be non-zero at points that are within a distance ϵ from the extrapolated interface. For very small contact angles, many cells left of the contact line and adjacent to the wall will be within this distance, and an (artificial) force on the fluid in these points would result from the finite thickness of the extrapolated interface. But since d at these points corresponds to the (signed) distance function from the extrapolated interface (a straight line), the curvature, and therefore the source term in the momentum equation, is actually zero in this region. This may be a desirable (but fortunate) effect of using a straight-line as the extrapolated interface. In Fig. 2, we see that the source term is indeed abruptly cut off just left of the contact line (the same trend was found for a smaller angle, $\theta = 2.5°$). An undesired side-effect is that the source term is seen to be somewhat disturbed at the mesh point at which this transition between regions of zero and non-zero curvature occurs. This was only found to occur at a single mesh point (also for finer meshes). In order to remove these artifacts, which occur only at contact angles close to 0° and 180°, a different extrapolated interface shape would have to be used.

With regard to points right of the contact line, the second-order extrapolation of d used there may lead to a distortion in the curvature close to the wall. The curvature is defined as $\nabla \cdot \mathbf{n}$ (where $\mathbf{n} = (n^1, n^2) = (\nabla\phi)/|\nabla\phi|$ is the local normal vector of the interface), which involves evaluation of second-order derivatives of d. Some deviation in the curvature was indeed observed in cells adjacent to the wall in regions where extrapolation of d to ghostcells was used. As mentioned above, however, this would only have an effect on the

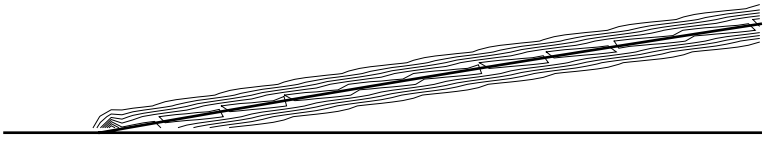

Fig. 2. Isocontours of the upward component of surface-tension source term in the momentum equation for a circular droplet. The distance to the horizontal axis is half of the grid spacing.

results if these points are sufficiently close to the interface. The deviation would be expected to be most significant for very small or very large contact angles: otherwise, the normalizing factor $|\nabla\phi|$ in $\mathbf{n}$ (used to determine the curvature) would be dominated by derivatives along the wall, which should not be affected strongly by extrapolation into the wall. On the other hand, at small or large θ, the curvature is necessarily small anyway. We see from Fig. 2 that for $\theta = 10°$, right of the contact line the source term in the momentum equation in the cells adjacent to the wall appears to be reasonably consistent with that in the rest of the interior.

4. Convergence tests

We consider here two cases of a droplet that is immersed in a different fluid, and adhering to a long boundary of a rectangular domain (2×1, discretisation is $2N \times N$). The fluid properties used in these cases are listed in Table 1. In Case I, the densities are equal whereas the viscosities differ; a density contrast is used in Case II. The sliplength is set to $\lambda = 0.02$. The corresponding maximum capillary number in Case I is $\mu U^{\mathrm{cl}}(t = 0)/\sigma = 6.74 \times 10^{-2}$ and Reynolds number $\rho H U^{\mathrm{cl}}/\mu = 6.731$ (based on initial droplet height H). The droplets are circular caps initially (radius 1.66), and the contact angles are $\theta_{1,2} = 30°$, which is different from the static contact angle $\theta_s = 120°$. The contact-line speed is prescribed in both cases, with $\kappa = 0.1$ in (3). As a result of (3), the contact lines start to move, until $\theta_{1,2} = 120°$. The qualitative flow features for this problem are discussed in detail in Section 5. Results for the convergence of the velocity and level-set function fields are given in Table 2, in terms of

$$E_N(U_i;t) = \int |(U_i)_N(\mathbf{x},t) - (U_i)_{N/2}(\mathbf{x},t)|\,\mathrm{d}A, \tag{20}$$

and a corresponding expression for $E_N(H(\phi);t)$, where $H(\phi)$ is the Heaviside function. The convergence rate is, for a $2N \times N$ mesh, defined as $\log_2(E_N^P/E_{2N}^P)$. Also given in Table 2 are the convergence rates of the time-integrated difference in the perimeter ($|P_N(t) - P_{2N}(t)|$) and contact angles of a droplet for different mesh sizes.

Unlike the single-phase version, the method for two-phase flow is obviously not second-order accurate (it was checked that the method is second order for single-phase flows by testing against an analytical

Table 1
Cases considered. A subscript '1' refers to the fluid of the droplet/bubble, '2' to the exterior fluid

	ρ_1	ρ_2	μ_1	μ_2	σ
Case I	1	1	4.95×10^{-2}	4.95×10^{-3}	0.11
Case II	1	20	4.95×10^{-2}	4.95×10^{-2}	2.21
Case III	1	0.05	1	0.05	100

Table 2
Convergence rates for the integrated difference in velocity components and $H(\phi)$ between successive approximations, and the time-integrated perimeter P and contact angle θ_1

	U_1	U_2	$H(\phi)$	P	θ
Case I, 128×64	0.61	0.71	1.1	1.9	2.2
Case I, 256×128	0.88	0.95	1.1	0.71	0.97
Case II, 128×64	2.3	2.2	0.89	1.5	0.83
Case II, 256×128	1.1	1.2	1.1	0.88	1.1

'decaying vortices' solution of the unsteady Navier–Stokes equations). This is not caused by the presence of contact lines; tests for a bubble rising in a box gave similar results.

The method is not expected to be second-order accurate, because of the redistance step: in (15), $\gamma = \Delta x$ reduces the convergence rate. A second-order accurate redistance would be required for an overall second-order method. Furthermore, Aleinov et al. [1] showed that their method (they used a different redistance step) is only second-order overall if the two fluids have equal density and viscosity values. This must be due to the fact that errors in ϕ are amplified when taking spatial derivatives of the viscosity (in (7)) and density (in (9)) (see (5) and (6)).

5. Results and comparison with other work

A widely studied problem with contact lines is the deformation of a droplet in a creeping shear flow [8,18,24,31]. In Fig. 3, the method is tested against boundary-element simulations of Schleizer and Bonnecaze [24] (their Fig.10b). The problem addressed here is a droplet that adheres to the long (bottom) wall of a rectangular geometry, with pinned contact lines ((3) with $\kappa = 0$). The droplet is a circular cap, has unit area (defining the unit length as half the channel width), and the initial contact angles are 60°. The viscosity and density of the droplet are equal to that of the surrounding fluid. The opposite (top) wall moves at speed $U_0 = 1$. The surface tension coefficient σ is such that the capillary number $\mu H U_0/\sigma = 0.1$, where H is the initial droplet height. The droplet is deformed by the flow, and reaches a steady-state shape. In the present method, the timestep restriction for very viscous fluids is severe. Therefore, the unsteady Stokes equations were used instead for this case. Also shown in Fig. 3 is the analogous comparison for a pressure-driven flow considered by Schleizer and Bonnecaze [24].

We study in Figs. 4–6 in more detail the flow corresponding to Case I in Section 4 (see also Table 1), for a droplet relaxing from $\theta_{1,2} = 30°$ to its static contact angle of 120°. The contact angles and perimeter are given as a function of time in Fig. 4. Also shown in Fig. 4 (by the dashed line) is the value that the perimeter would have had, had the interface been a circular cap, with $\theta_{1,2}(t)$ equal to the actual values. It is seen that for $t \geqslant 5$, this coincides with the actual perimeter, showing that for these longer times the contact lines have slowed down enough for the interface to be a circular cap. This regime is dominated by the contact-line law (3). It was found that the initial period, during which the interface is not circular, is sensitive to the value of λ.

A snapshot of the contact-line region during this initial period is shown in Fig. 5, in a frame moving with the left contact line. The flow inside the drop is seen to be of the expected wedge-flow type. Outside the drop, the fluid moves along the interface together with the wedge flow inside, away from the contact line.

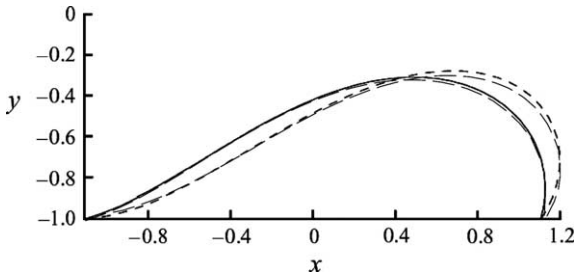

Fig. 3. Comparison against results of Schleizer and Bonnecaze (reproduced with permission from Cambridge University Press from [24]), who used a boundary-element method. The solid and short-dashed lines correspond to their results for pressure-driven and shear flow, respectively. The long dashes indicate the present results, using a 128×32 grid.

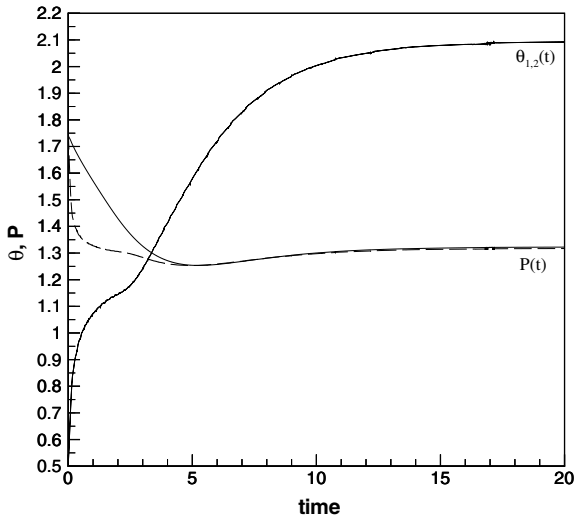

Fig. 4. Perimeter P and contact angles as a function of time for a droplet with moving contact lines in a fluid without external flow. Case I: relaxation from initial contact angles of 30°, to the static contact angle of 120°. The long-dashed line represents the perimeter for an exact circular interface with contact angles corresponding to the values resulting from the simulations.

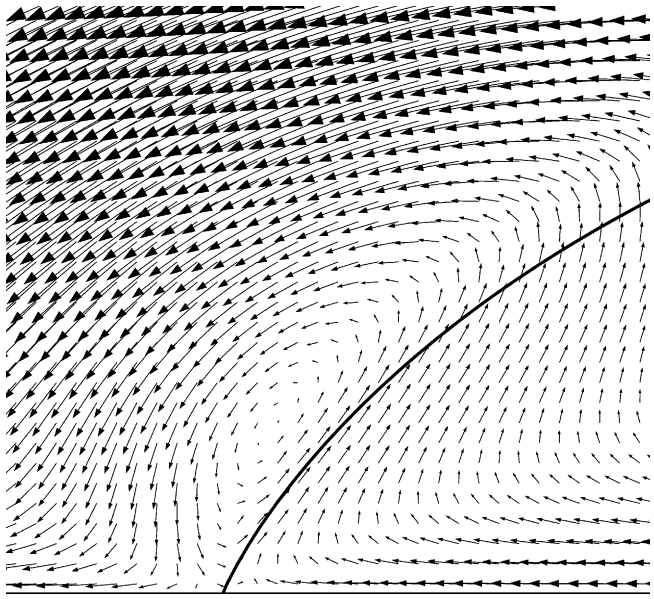

Fig. 5. Detail of the flow near the left contact line (in a frame moving with the contact line) at $t = 1.62$, also showing the velocity field.

The exterior fluid flows towards the contact line under an angle, which is in qualitative agreement with the flow patterns observed by Dussan V. and Davis [10]. This exterior fluid inflow is supplied by a vortical structure, caused by the upward motion of the central part of the drop.

In order to investigate the regularisation of the stress singularity, the shear rate $\partial U_1/\partial x_2$ along the wall is shown in Fig. 6. In Fig. 6(a), results are shown for $\lambda = 0$, for different mesh sizes. We see that the maximum shear rate increases rapidly with mesh refinement, apparently not converging, consistent with a stress

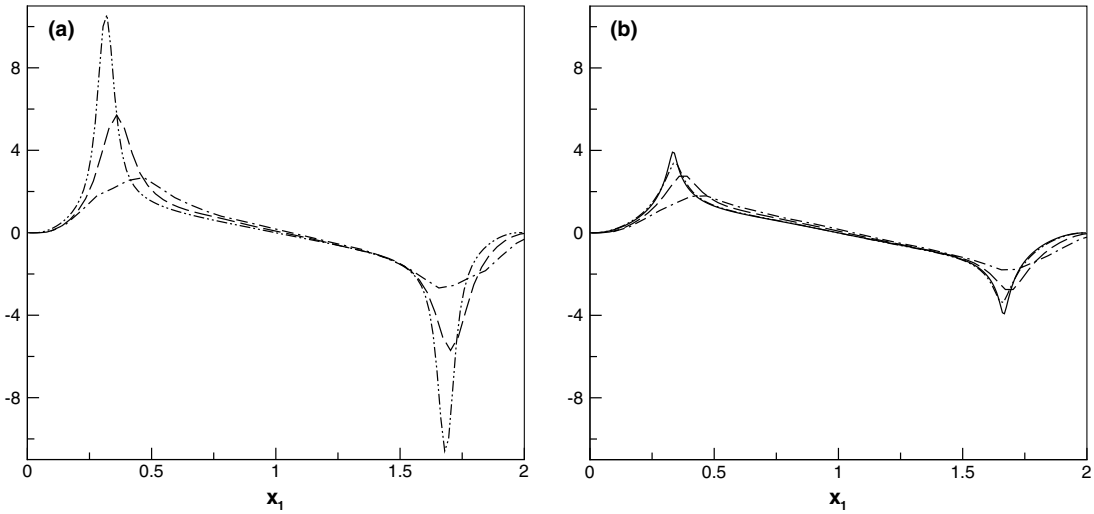

Fig. 6. Shear rate $\partial u_1/\partial x_2$ at the wall for a droplet with moving contact lines in a fluid without externally imposed flow (Case I). No-slip condition (a) or slip with $\lambda = 2 \times 10^{-2}$ (b) is applied along the entire wall. Results shown are for mesh sizes 32×16 (–·–), 64×32 (––), 128×64 (–··–) and 256×128 (solid line; slip case only).

singularity. In Fig. 6(b), the corresponding results are shown for $\lambda = 0.02$ in the slip condition (1) along the entire wall. The peaks in the shear-rate at the contact lines are reduced significantly, and appear to be converging as the mesh is refined.

The interface shape for a spreading droplet in the viscous bending regime is shown in Fig. 7 (Case III in Table 1, with (2), $\theta_A = 10°$, initial large-scale contact angle of 40°, $\theta_R = 0$, $\lambda = 0.01$). In these simulations,

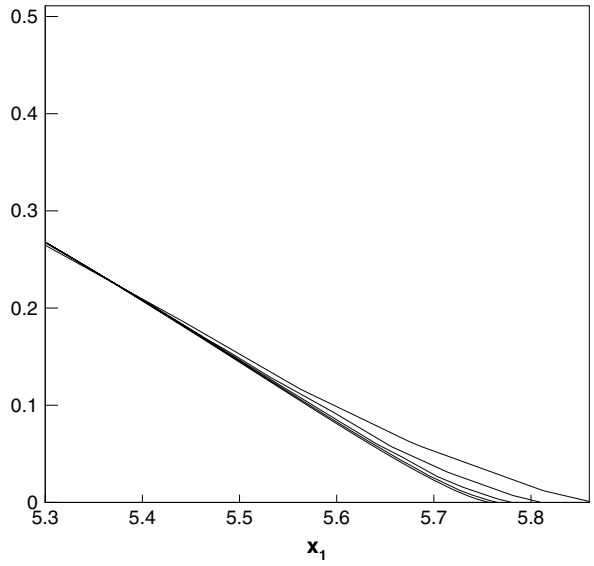

Fig. 7. Dependence of interface shape on grid spacing in the contact-line region, using (2) with $\theta_A = 10°$, $\theta_R = 0$, $\lambda = 0.01$ for Case III; drop area is 1.5, initial (large-scale) contact angles are 40°. The contact line is moving to the right. N is (for interfaces from right to left) 8, 16, 32, 64 and 128, respectively.

the total domain dimensions are 8×1, and the mesh size is $8N \times N$. The results appear to converge for small grid spacing. Using a coarse mesh is seen to increase the size of the region in which the bending occurs, as well as the contact-line speed. This is consistent with the expectation that a coarse mesh leads to a larger effective slip coefficient.

A lubrication theory for two-dimensional droplet spreading has been presented by Hocking [13]. For very small sliplengths, he showed that the solution of the flow on a macroscale (away from the contact-line region) can be matched to the solution for the contact-line region by introducing an intermediate region, provided that

$$\theta_d^3 = \theta_A^3 + 9Ca^{cl} \ln\left(\frac{h_m}{\lambda}\right), \tag{21}$$

where $Ca^{cl} \equiv \mu_1 U^{cl}/\sigma$, θ_d is an apparent contact angle, associated with the large-scale flow, and

$$h_m = 2a\theta_A/(3e^2) \tag{22}$$

(a is the instantaneous drop radius). A similar result, but more generally valid, has been derived in [5], which has been compared to experiments by Foister [11], amongst others. For very thin droplets, such that the (constant) drop area is θa^2, (21) also agrees approximately with Tanner's experiments [29] for the two-dimensional case, in which $a \sim t^{\frac{1}{7}}$ if $\theta \gg \theta_A$.

For (21) to be applicable, λ must be very small, making $1/\ln(h_m/\lambda)$ a small parameter. Nevertheless, a relation of the type (21) may be expected to be valid at larger λ (in [19], $h_m/\lambda = 8$). The apparent angle θ_d has been associated with the maximum tangential angle of the interface, θ_{max} [30], although [13] cautioned that using (21) in a higher-order approximation destroys the validity of the concept of an apparent contact angle.

An estimate of θ_{max} was obtained in the present simulations from the reconstruction of the interface, using bilinear interpolation. Results presented here are for the average values of θ_{max} and Ca^{cl}, over the time it took the contact line to move a distance $4\Delta x$. Averaging was necessary, because determining U^{cl} requires time-differentiation of the contact-line position, and small jumps in contact-line position occur when the contact line moves into a new grid cell. The resulting dependence of θ_{max} on Ca^{cl} is shown in Fig. 8(a) for $\lambda = 0.01$ and different grid spacings, and in Fig. 8(b) for $\lambda = 0.005$, 0.01 and 0.02 (other parameters are as in Fig. 7). In order to compare the result against (21) and (22), it should be noted that this analytical result gives a dynamic contact angle for a droplet of half-length $a(t)$, spreading at dimensionless speed Ca^{cl}. In Fig. 8(b), (21) and (22) is represented by long dashes, a corresponding to a value of Ca^{cl} was obtained from simulations.

The simulation results in Fig. 8(a) approach the lubrication theory at low values of Ca^{cl}. A difference at larger capillary number may be caused by either the drop not being sufficiently thin for the lubrication theory to hold, or by the fact that (21) is a lowest-order approximation in the capillary number. It seems unlikely that 'numerical slip' is the cause, as the contact-line moves slower in the simulations than in the theory. The solid lines in the figure are for density and viscosity contrasts of 20, the long dashes for 40. It is seen that the exterior fluid hardly has any effect on the results for such contrasts. This is also consistent with experimental findings [11].

It is seen from Fig. 8(b) that the value of θ_{max} in the simulations is somewhat smaller than the result (21) and (22) for θ_d, especially at low values of Ca_{cl}. There is still some dependence on mesh size in the results (as is also clear from Fig. 8(a)): doubling the grid spacing for $\lambda = 0.005$ resulted in a downward shift in Fig. 8(b) by about 0.02. Using an even smaller grid spacing would require an excessive computational effort, whereas $\lambda = 0.02$ is already clearly too large for the lubrication theory to apply ((21) for larger values of λ results in an unphysical negative value of θ_d). The numerical simulations presented in [30], using the evolution equation for the drop height (obtained from lubrication theory), show that θ_{max} could be fitted well by an equa-

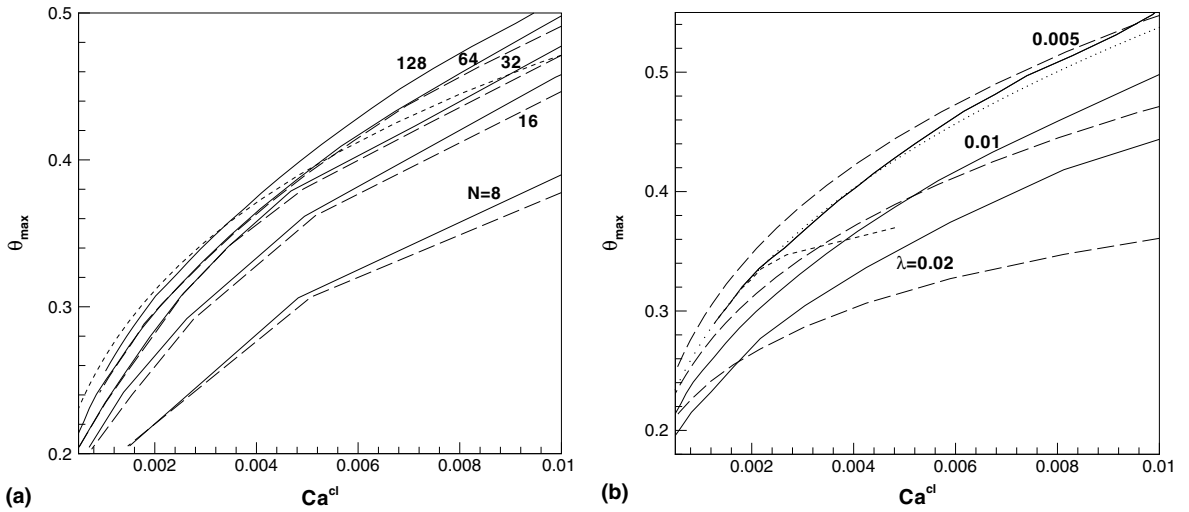

Fig. 8. (a) Maximum tangential angle of the interface as a function of Ca^{cl} for a spreading droplet, using different number of grid points. $\lambda = 0.01$ in all cases; other parameters as in Fig. 7 Results shown were obtained by averaging θ_{max} and Ca^{cl} over short time periods during the spreading process, in which the contact lines moved over a distance $4\Delta x$. The dashed line represents the result of lubrication theory, (21) and (22). The long dashes represent numerical results for a density and viscosity ratio of 40 instead of 20 ($N \leqslant 64$). (b) Maximum tangential angle of the interface as a function of Ca^{cl} for a spreading droplet. Results shown were obtained by averaging θ_{max} and Ca^{cl} over short time periods during the spreading process, in which the contact lines moved over a distance $4\Delta x$. Solid lines are simulation results for different sliplengths, with $\Delta x = \frac{25}{16}\lambda$ (other parameters as in Fig. 7). The short dashes represent simulation results for an initial contact angle of 23°. Long-dashed lines represent (21) and (22). The dotted line is (21) with the logarithmic term replaced by a fitted constant.

tion of the form (21) for a droplet sliding down a vertical plane, but with the logarithmic term replaced by a constant:

$$\theta_d^3 = \theta_A^3 + \alpha Ca^{cl}. \tag{23}$$

An example of such a fit is shown for $\lambda = 0.005$, which is seen to be an acceptable fit to the data. Overall, we can infer from Fig. 8 that there is reasonable agreement between simulations and lubrication theory.

Also shown in Fig. 8(b) is the simulation result for the same droplet using the smallest value of λ (=0.005), but with a smaller initial contact angle (23°). Apart from a short initial period (corresponding to the large-Ca^{cl} end of the results), the dynamic contact angle is seen to be virtually independent of initial conditions, as expected from the lubrication theory.

We present results for flows with moving contact lines that are not of conventional free-surface flow type in Fig. 9. In Fig. 9(a), the velocity field is shown for a bubble that moves along a wall, due to an imposed shear flow, using (3). The wake moves with the bubble. It is seen that, due to the rotational flow inside the bubble, the fluid makes a U-turn between the bubble and its wake, resulting in a wake some distance downstream. The time-evolution of the perimeter and contact angles is shown in Fig. 9(b). A small oscillation is observed in $\theta_{1,2}$, but the amplitude decreases if a finer mesh is used.

6. A macroscale approach for small sliplengths

It is clear from the results presented above that, for an accurate resolution of the flow, the grid spacing should be less than the sliplength. The results presented in Figs. 7 and 8 show that, for the case that the

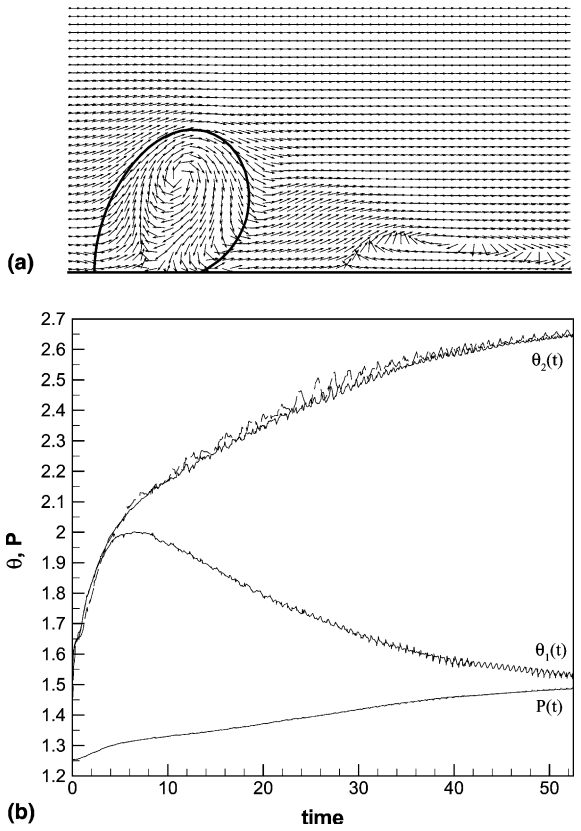

Fig. 9. (a) Velocity flags (indicating local direction of fluid velocity) for a bubble with moving contact lines in a shear flow (detail) with $\rho_1 = 1$, $\rho_2 = 20$, $\mu_1 = \mu_2 = 0.1592$, $\sigma = 3.175$. Initial contact angles are 90°; $\theta_s = 120°$, $\kappa = 0.1$, $\lambda = 0.04$. Simulations are approaching a quasi-steady state, in which the drop moves at constant speed without further deformation, for a 128×32 mesh. (b) Perimeter P and contact angles as a function of time. The dashed line corresponds to θ_2 when using a 64×16 mesh.

contact angle is prescribed, a mesh coarser than the sliplength leads effectively to too much slip. The 'slip' is provided by discretisation errors, since the velocity is not exactly prescribed at the wall because it is defined at cell centres, not cell vertices. This restricts the practical application of the present method to values of λ that are not so small that an unrealistically large mesh would be required (although local mesh refinement is of course an option [27]).

We test here the possibility of solving the flow on a macroscale only, as follows. For spreading droplets, the velocity of the contact line satisfies (21),

$$U^{\mathrm{cl}} = \left(\theta_d^3 - \theta_{\mathrm{A}}^3\right)\sigma \Big/ 9\mu \ln\left(\frac{h_m}{\lambda}\right). \tag{24}$$

Using this expression to integrate $X^{\mathrm{cl}}(t)$ has the advantage that the right-hand side contains only macroscale quantities. A similar approach would be to use (23), with α proportional to $\ln(1/\lambda)$, and to use simulations as in the previous section (for relatively large λ) to determine the proportionality factor. We shall combine these approaches here with still prescribing the corresponding value of θ_{A}.

In Fig. 10 the result for $\lambda = 5 \times 10^{-3}$ has been copied from Fig. 8(b), obtained from the 'full' simulations of the previous section. Also shown are results using the 'macroscale' approach of this section, in which (23)

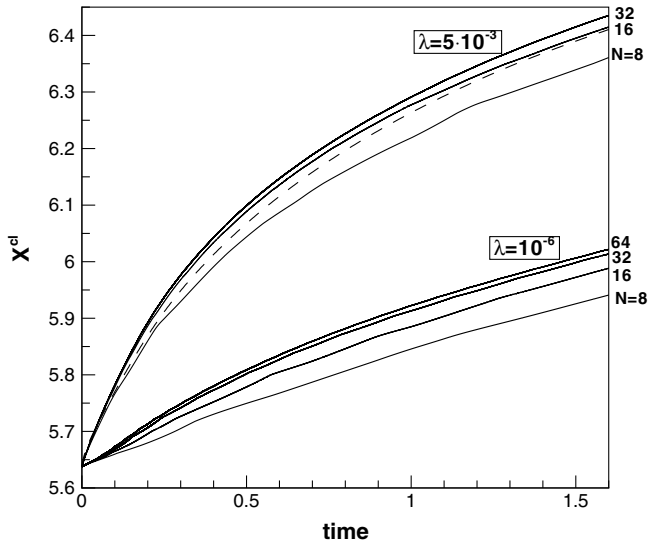

Fig. 10. Position of a contact line as a function of time for a spreading droplet, Case III. Solid lines represent solutions of the macroscale flow using (23) (for $\lambda = 5 \times 10^{-3}$) or (21) and (22) (for $\lambda = 10^{-6}$); the dashed is the result of a 'full' simulation using (1) and (2).

has been used, with the value of α obtained from the full simulation. The fit is shown in Fig. 8(b) for comparison; α was chosen such that especially the results for low values of Ca^{cl} are well represented (it is a lowest-order approximation in Ca^{cl}). The macroscale results for $X^{cl}(t)$ appear to converge to a value somewhat above the result from the full simulation. The difference has resulted during $t < 0.4$, which was found to correspond to values of $\theta_m > 0.46$. From Fig. 8(b) we can conclude that the difference may be attributed to a small error in the fit (23), which for this value of α overpredicts the contact-line speed.

This result indicates that a macroscale approach can be used to determine spreading rates. The second set of results shown in Fig. 10 are for a realistic value of λ ($=10^{-6}$), using (24). Again, the results appear to converge rapidly, despite the small value of λ.

7. Discussion

A level-set approach has been proposed for the simulation of flow with moving contact lines that accounts for effects of inertia, contact-line hysteresis and slip. The method is shown to converge, and to agree with previous work. The technique proposed here does not use discretisation errors to introduce slip [19,20], the sliplength is imposed explicitly instead.

A macroscale approach has been suggested for the simulation of flows with very small values of λ. Alternatively, local mesh refinement may be used, although this has not been pursued here (the level-set method of Sussman et al. [27] facilitates local mesh refinement). The macroscale approach assumes that (3) (or (24)) represents the solution of the contact-line region, where θ (resp. θ_d) is the macroscopic contact angle. The grid spacing is then assumed to be much larger than λ. Such an approach may be justifiable in practical cases, since Cox [5] derived, under fairly general conditions, a relation between the contact-line speed, macroscopic and microscopic contact angles that is similar to (3), with κ dependent on $\ln \lambda^{-1}$ (see (24)). In such an approach, relaxation effects [4,25] could also be taken into account, since these lead to relations similar to (24), with the right-hand side depending on additional parameters.

Acknowledgement

The author thanks Thomas Selerland for introducing him to the level-set method.

References

[1] I.D. Aleinov, E.G. Puckett, M. Sussman, Formation of droplets in microscale jetting devices, in: Proceedings of the 3rd ASME/JSME Joint Fluids Engineering Conference, 1999, FEDSM99-7106.
[2] A.S. Almgren, J.B. Bell, W.G. Szymczak, A numerical method for the incompressible Navier–Stokes equations based on an approximate projection, SIAM J. Sci. Comput. 17 (1996) 358–369.
[3] A.L. Bertozzi, The mathematics of moving contact lines in thin liquid films, Notices AMS 45 (1998) 689–697.
[4] J. Billingham, A reappraisal of a new model for the motion of a contact line on a smooth solid surface (submitted).
[5] R.G. Cox, The dynamics of the spreading of liquids on a solid surface. Part 1. Viscous flow, J. Fluid Mech. 168 (1986) 169–194.
[6] S.H. Davis, in: G.K. Batchelor, H.K. Moffatt, M.G. Worster (Eds.), Perspectives in Fluid Dynamics, Cambridge University Press, Cambridge, 2002.
[7] P.G. de Gennes, Wetting: statics and dynamics, Rev. Mod. Phys. 57 (1985) 827–863.
[8] P. Dimitrakopoulos, J.J.L. Higdon, On the displacement of three-dimensional fluid droplets adhering to a plane wall in viscous pressure-driven flows, J. Fluid Mech. 435 (2001) 327–350.
[9] E.B. Dussan V., On the spreading of liquids on solid surfaces: static and dynamic contact lines, Annu. Rev. Fluid Mech. 11 (1979) 371–400.
[10] E.B. Dussan V., S.H. Davis, On the motion of a fluid–fluid interface along a solid surface, J. Fluid Mech. 65 (1974) 71–95.
[11] R.B. Foister, The kinetics of displacement wetting in liquid/liquid/solid systems, J. Colloid Interface Sci. 136 (1990) 266–282.
[12] L.M. Hocking, Sliding and spreading of thin two-dimensional drops, Q. J. Mech. Appl. Math. 34 (1981) 37–55.
[13] L.M. Hocking, The motion of a drop on a rigid surface, in: Proceedings of the 2nd International Colloquium on Drops and Bubbles, 1982, pp. 315–321.
[14] L.M. Hocking, Rival contact-angle models and the spreading of drops, J. Fluid Mech. 239 (1992) 671–681.
[15] D. Jacqmin, Contact-line dynamics of a diffuse fluid interface, J. Fluid Mech. 402 (2000) 57–88.
[16] S. Kalliadasis, H.-C. Chang, Apparent dynamic contact angle of an advancing gas–liquid meniscus, Phys. Fluids 6 (1994) 12–23.
[17] Q. Kang, D. Zhang, S. Chen, Displacement of a two-dimensional immiscible droplet in a channel, Phys. Fluids 14 (2002) 3203–3214.
[18] X. Li, C. Pozrikidis, Shear flow over a liquid drop adhering to a solid surface, J. Fluid Mech. 307 (1996) 167–190.
[19] A. Mazouchi, C.M. Gramlich, G.M. Homsy, Time-dependent free surface Stokes flow with a moving contact line. I. Flow over plane surfaces, Phys. Fluids 16 (2004) 1647–1659.
[20] J.A. Moriarty, L.W. Schwartz, Effective slip in numerical calculations of moving-contact-line problems, J. Eng. Math. 26 (1992) 81–86.
[21] A. Oron, S.H. Davis, S.G. Bankoff, Long-scale evolution of thin liquid films, Rev. Mod. Phys. 69 (1997) 931–980.
[22] M. Renardy, Y. Renardy, J. Li, Numerical simulation of moving contact line problems using a volume-of-fluid method, J. Comput. Phys. 171 (2001) 243–263.
[23] G. Russo, P. Smereka, A remark on computing distance functions, J. Comput. Phys. 163 (2000) 51–67.
[24] A.D. Schleizer, R.T. Bonnecaze, Displacement of a two-dimensional immiscible droplet adhering to a wall in shear and pressure-driven flows, J. Fluid Mech. 383 (1999) 29–54.
[25] Y.D. Shikhmurzaev, Moving contact lines in liquid/liquid/solid systems, J. Fluid Mech. 334 (1997) 211–249.
[26] G. Son, V.K. Dhir, N. Ramanujapu, Dynamics and heat transfer associated with a single bubble during nucleate boiling on a horizontal surface, J. Heat Transfer 121 (1999) 623–631.
[27] M. Sussman, A.S. Almgren, J.B. Bell, P. Colella, L.H. Howell, M.L. Welcome, An adaptive level set approach for incompressible two-phase flows, J. Comput. Phys. 148 (1999) 81–124.
[28] M. Sussman, S. Uto, A computational study of the spreading of oil underneath a sheet of ice, CAM Report 98-32, 1998.
[29] L.H. Tanner, The spreading of silicone oil drops on horizontal surfaces, J. Phys. D 12 (1979) 1473–1483.
[30] E.O. Tuck, L.W. Schwartz, A numerical and asymptotic study of some third-order ordinary differential equations relevant to draining and coating flows, SIAM Rev. 32 (1990) 453–460.
[31] S. Yon, C. Pozrikidis, Deformation of a liquid drop adhering to a plane wall: significance of the drop viscosity and the effect of an insoluble surfactant, Phys. Fluids 11 (1999) 1297–1308.